Draft version November 11, 2021
Typeset using LaTeX **modern** style in AASTeX62

A study of sunspot 3 minute oscillations using ALMA and GST

Yi Chai,[1] Dale E. Gary,[1] Kevin P. Reardon,[2,3] and Vasyl Yurchyshyn[4]

[1] *Center for Solar-Terrestrial Research*
New Jersey Institute of Technology
Newark, NJ 07102, USA
[2] *National Solar Observatory, Boulder, CO, 80303*
[3] *Department of Astrophysical and Planetary Sciences, University of Colorado, Boulder, CO, 80303*
[4] *Big Bear Solar Observatory, Center for Solar-Terrestrial Research*
New Jersey Institute of Technology
Newark, NJ 07102, USA

(Received; Revised; Accepted)

Submitted to ApJ

ABSTRACT

Waves and oscillations are important solar phenomena, not only because they can propagate and dissipate energy in the chromosphere, but also because they carry information about the structure of the atmosphere in which they propagate. The nature of the three-minute oscillations observed in the umbral region of sunspots is considered to be an effect of propagation of magnetohydrodynamic (MHD) waves upward from below the photosphere. We present a study of sunspot oscillations and wave propagation in NOAA AR 12470 using an approximately one-hour long data set acquired on 2015 December 17 by the Atacama Large Millimeter/submillimeter Array (ALMA), the Goode Solar Telescope (GST) operating at the Big Bear Solar Observatory (BBSO), the Atmospheric Imaging Assembly (AIA) on board the Solar Dynamics Observatory (SDO), and the Interface Region Imaging Spectrograph (IRIS). The ALMA data are unique in providing a time-series of direct temperature measurements in the sunspot chromosphere. The two-second cadence of ALMA images allows us to well resolve the three-minute periods typical of sunspot oscillations in the chromosphere. Fourier analysis is applied to ALMA Band 3 (∼100 GHz, ∼3 mm) and GST Hα data sets to obtain power spectra as well as oscillation phase information. We analysed properties of the wave propagation by combining multiple wavelengths that probe physical parameters of solar atmosphere at different heights. We find that the ALMA temperature fluctuations are consistent with that expected for a propagating acoustic wave, with a slight asymmetry indicating non-linear steepening.

Keywords: Chromosphere, Sunspot, Oscillation

1. INTRODUCTION

Sunspot oscillations are a frequently studied wave phenomenon in the solar atmosphere. These oscillations are directly connected with the propagation of solar magnetohydrodynamic (MHD) waves and may play a role in coronal and chromospheric heating. Moreover, they can also serve as a probe of the structure of the solar atmosphere. Oscillations in sunspot umbrae (e.g., Beckers & Tallant 1969; Beckers & Schultz 1972; Giovanelli 1972) were reported shortly after the discovery of p-mode oscillations. There are two types of characteristic oscillations in sunspots, the photospheric 5-minute oscillations driven by the p-modes and 3-minute oscillations rep-

Corresponding author: Yi Chai
yc389@njit.edu

resenting the resonant mode of the sunspot itself (Thomas 1981; Bogdan & Judge 2006; Khomenko & Collados 2015).

Studies of sunspot oscillations have been carried out by multiple instruments over the years, including the Solar Optical Telescope onboard Hinode (Nagashima et al. 2007), the Nobeyama Radioheliograph (Reznikova et al. 2012), the Atmospheric Imaging Assembly on board SDO (Reznikova et al. 2012; Sych & Nakariakov 2014), the Interface Region Imaging Spectrograph (Tian et al. 2014; Yurchyshyn et al. 2015), the Goode Solar Telescope (GST) operating at Big Bear Solar Observatory (BBSO) (Maurya et al. 2013; Yurchyshyn et al. 2015; Su et al. 2016) and other ground-based telescopes (e.g., Centeno et al. 2006; Löhner-Böttcher et al. 2016; Anan et al. 2019; Felipe et al. 2020).

The sunspot oscillations are a specific manifestation of the significant amount of acoustic energy generated through oscillatory motion in near-surface layers. In the upper photosphere, most of the upward propagating waves at lower frequencies (below 5 mHz, or periods longer than 3-4 minutes) are reflected back downward while higher frequency waves continue to propagate upward into the chromosphere. A variety of observations have revealed how energy is deposited in the upper atmosphere due to such wave motions. For example, a study by Reardon et al. (2008) using Ca II (854.2 nm) line observations from the Interferometric Bidimensional Spectrometer (IBIS) revealed the presence of a power-law distribution of significant oscillatory power up to 25 mHz, suggestive of the widespread presence of turbulence from shock dissipation in the chromosphere.

Waves also carry information about the structure of the atmosphere in which they propagate. Since the sound speed is a function of temperature in the chromosphere, pressure disturbances with frequencies above the acoustic cut-off frequency can provide direct information about the atmosphere at different heights and the accompanying temperature and velocity perturbations.

Over many years, numerous efforts have being made in studying the particular oscillatory signals seen in sunspot umbrae. Using Hα filters on the 12 inch solar telescope in Culgoora, Giovanelli (1972) was the first to measure sunspot oscillations in Hα velocity. Later on, more detail has been revealed using Hα line wing data. Phillis (1975) showed the intensity variation in red and blue wings of Hα at $\pm$0.3Å that demonstrate the line-of-sight velocity field as an oscillation on a upward flow. Uexkuell et al. (1983) compared the oscillations measured from several lines (Ca II, Na D1 and D2, Ni I, Hα) using power spectra analysis and studied the phase relation between them. With the high cadence filtergrams from Universal Birefringent Filter on the Dunn Solar Telescope (DST), Christopoulou et al. (2000, 2001) studied the relation between running penumbra waves and umbral oscillations in different layers of the solar atmosphere marked by different lines from Hα line center and wings. Tziotziou et al. (2007) studied multiple umbral flashes in one sunspot using Ca II and Hα intensity images and revealed the coexistence of more than one oscillating mode, suggesting different physical conditions existing in the umbra.

However, studies of wave propagation in the chromosphere are not straightforward. For example, Mein & Mein (1976) and Fleck & Deubner (1989) found no phase difference between the Doppler shifts of the Ca II infrared triplet lines at 854.2 nm and 849.8 nm, which are formed at different heights, and used this as evidence of a non-propagating component in the chromospheric wave field. However, this conclusion was questioned by Skartlien et al. (1994), whose simulations of propagating disturbances predicted little or no phase difference between these lines, similar to the above observations, even though propagating shocks were present. This shows that in interpreting observations it is necessary to consider the radiative transfer effects and the atmospheric structure over the entire range of heights contributing to the observed emissions.

Previous observations have shown the capability of detecting oscillations in sunspots using radio instruments such as the Nobeyama Radio Observatory (Shibasaki 2001) and the Very Large Array (Nindos et al. 2002). Loukitcheva et al. (2004) has demonstrated the feasibility of measuring chromospheric oscillations in the mm range. Such observations have the distinct advantage of directly probing the plasma temperature at different heights in the solar chromosphere depending on the observing frequency.

Early research (Leibacher & Stein 1981; Zhugzhda & Dzhalilov 1982; Zhugzhda 1984) on the oscillations in the chromosphere suggested that the oscillatory modes are produced by a resonant cavity. However, in more recent studies (Felipe et al. 2010; Chae & Goode 2015), a different scenario has been proposed that the 3 minutes oscillation is a direct indication of vertically propagating waves that travel through the gravitationally stratified medium. Despite the growing knowledge and complexity of theoretical models, there remain several open questions related with the fundamental physical mechanisms in the sunspot region.

The need for better understanding of the fine structure of the 3 min oscillation and its time evolution in sunspots has intensified with the development of better observating tools. Among modern observatories, the Atacama Large Millimeter/submillimeter Array (ALMA) opens up a new era of solar radio observation due to its high spatial and temporal resolution and image quality (e.g. Nindos et al. 2018; Molnar et al. 2019; Nindos et al. 2021). When combined with other cutting-edge instruments, such as BBSO/GST, SDO/AIA and IRIS, ALMA can provide unique electron temperature diagnostics that clarify the behavior of the solar chromosphere to propagating waves (see Patsourakos et al. 2020; Nindos et al. 2021, for a discussion of p-mode oscillations seen with ALMA).

The aim of this paper is to present an analysis of 3-minute oscillations in a sunspot umbra using data gathered by multiple instruments and demonstrate the presence of such oscillatory motion in ALMA Band 3 data. With the help of high-cadence and high-resolution ALMA data as well as the linear dependence between ALMA image intensity and brightness temperature of the plasma (Wedemeyer et al. 2016), we report some of the first observations of spatially resolved temperature oscillations in a sunspot umbra.

2. OBSERVATIONS

We analysed the oscillation signal measured in the western part of active region NOAA 12470 during one-hour observing period (18:42 UT – 19:48 UT on 2015 December 17), which was part of an ALMA solar commissioning campaign whose data are in the public domain. The ALMA dataset we used was provided by the ALMA observatory as part of its Science Verification data release. Previous publications based on this ALMA data release are Bastian et al. (2017), Iwai et al. (2017), Loukitcheva et al. (2017), and Shimojo et al. (2017). Only Shimojo et al. (2017) used data from the same day (2015 December 17) as considered here, and that study was focused on a small brightening rather than the sunspot itself. Our observations were conducted using the band 3 receiver (centered at 100 GHz) in a single-pointing (snap-shot) mode. Due to the necessity of phase calibration, blocks of on-target observations were run for approximately 615 s at a cadence of 2 s, followed by a 220-s off-target phase calibrator scan, which resulted in total of five solar scans to be analyzed. In this paper, we will use designations $t1$, $t2$, $t3$, $t4$, and $t5$ to represent each solar scan arranged in time increase order. The ALMA antenna configuration consisted of total 31 antennas with twenty two 12-m antennas and nine 7-m antennas. The longest baseline of the antenna configuration was ∼300 m, which resulted in a synthesized beam of $6.3'' \times 2.3''$ (Shimojo et al. 2017).

We followed the general calibration method of radio interferometry using the Common Astronomy Software Applications (CASA) package (Petry & CASA Development Team 2012) to create images at 2 s cadence, and found that the result is heavily influenced by phase errors produced by the temporal and spatially variable water content of the Earth's atmosphere, which can be severe enough to render sunspot oscillations undetectable. In order to counter this effect, we carried out a self-calibration process, which uses the solar signal itself to correct for antenna-based phase and amplitude errors, similar to a method by Shimojo et al. (2017).

The scheme of self-calibration can be described as follows: a) split the data that have been corrected using standard calibration into 10 min sub-datasets $t1$-$t5$ according to the scan index. b) For each sub-dataset, make an image from the entire 10-min period using the *CLEAN* task in CASA, to use as a model for self-calibration. The model is stored in the dateset for later use. Atmospheric fluctuations will largely average out in such a long integration. c) Determine phase corrections for each 2-s time period relative to the model given by step b using the *gaincal* task in CASA,

and generate a self-calibration table. d) Apply the phase corrections to each image in the sub-dataset using the *applycal* task in CASA and generate an intermediately corrected sub-dataset. e) Iteratively repeat steps b-d, substituting in each intermediate sub-dataset, until no further correction is needed, as determined by checking the calibration table for reduction of the residuals.

In our case, we applied this phase self-calibration cycle four times, resulting in final residual phase fluctuations of around 10 degrees standard deviation. We applied the scheme to each of the measured 10-min sub-datasets to complete the self-calibration procedure. The result shows a clear improvement in removing the fluctuations caused by the Earth's atmosphere and allows the regular variations due to sunspot oscillations to be measured.

The smallest spatial scale of the antenna configuration is roughly 70″, which is not sufficient to measure the solar background brightness temperature over the band 3 field of view (FOV; ∼80″ in Figure 1). To overcome this drawback, the single-dish observations of the full Sun were taken using three other antennas to measure the overall emission close in time to when ALMA was observing the target (White et al. 2017). The information from both interferometer and single-dish antennas then were combined using the "feathering" process in CASA to obtain the true temperature scale on the full-range of spatial scales. The left panel of Figure 1 shows the end result of this full process, which has a pixel scale of 0.3″ and FOV as defined by the interferometer images. The field of view is truncated at the 20% level of the peak response of the primary (single-dish) beam and has been corrected for the declining antenna response, which becomes more extreme near the edges.

Due to the fact that ALMA is using the equatorial coordinate system (RA-Dec) as the output framework for its data sets, as part of the image processing we performed a coordinate transformation to heliocentric coordinates, to align the ALMA images with those from other solar instruments. In this procedure, the center of the field of view (FOV) of each solar image in one scan was transformed based on the heliocentric coordinates at the mid-time of the scan to align all of the images to a fixed time. A time dependent rotation was applied to take into account the rotation between these two frames, leaving the images aligned with solar north.

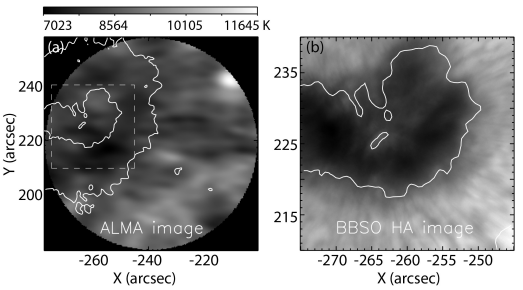

Figure 1. (a) ALMA brightness temperature image with contours from HMI continuum image showing the umbral and penumbral boundary of sunspot AR12470 at 19:02 UT. The box marked with a dashed line shows the FOV of the BBSO GST Hα image in the right panel. (b) GST Hα near blue wing (-0.4 Å) image with the same HMI umbral contour.

To compare the ALMA images with those at other wavelengths, we obtained the UV and EUV intensity data cube from the Atmospheric Imaging Assembly (AIA) on board the Solar Dynamics Observatory (SDO) (Lemen et al. 2012) in the bandpass of 171 Å (Fe IX: the quiet corona) and 304Å (He II: the chromosphere and transition region). The time cadence of these two data sets is 12 s and the pixel resolution is 0.6″. The duration of the AIA data we used covers the full ALMA solar observation from 18:42 UT to 19:48 UT. Images of both wavelengths were extracted from the full-disk data to fit the FOV of ALMA and the center coordinates of these images were shifted to correct for solar rotation. The continuum intensity data product from by the Helioseismic and Magnetic Imager (HMI) on SDO was used for alignment of between the SDO and GST images.

The Goode Solar Telescope (GST) operating at BBSO (Cao et al. 2010) observed this AR nearly simultaneously with ALMA (from 18:50 UT to 20:59 UT) at Hα line-center and off-band wavelengths (±0.4 Å and ±0.8 Å) using the Visible Imaging Spectrograph (VIS) instrument. The spatial scale of the GST Hα images is 0.034″ per pixel, the VIS bandwidth is 0.08 Å, and the time cadence was 40 s. Speckle reconstruction is normally performed by taking 100 frames in rapid succession and apply-

ing the algorithm to obtain a single sharper image. However, this algorithm can produce occasional glitches in low-light regions such as sunspot umbrae, which are the focus of our study. Since high spatial resolution is not needed for large-scale features of umbral oscillations, the unreconstructed Hα images were used. The GST observations cover the entire ALMA observing period $t2$–$t5$ but are missing the first few minutes during $t1$ set. Since our interest is on the joint ALMA-GST coverage, we mainly focus on analysing the $t2$–$t5$ ALMA sub-datasets.

We also used the slit-jaw images in Mg II k band (2796 Å) from the Interface Region Imaging Spectrograph (IRIS) which is formed in the chromosphere (De Pontieu et al. 2014) as a comparison to the ALMA temperature oscillation. IRIS started observations during $t3$ and suffered some cosmic-ray noise during the first 10 minutes, which can be seen later in the time-distance plots.

3. ANALYSIS

To visualize the oscillatory motion in the sunspot in various wavelengths, we show in Figure 2 time-distance plots along a line (Figure 2h) that crosses both umbra and penumbra. The double solid lines in Figure 2h mark the width of the slit over which the data are summed, with an ALMA map for reference, overlaid with HMI contours that mark the boundaries of the umbra and penumbra. The time-distance plots were constructed for each wavelength after co-alignment, as shown in the other panels of Figure 2. The y coordinate in each plot corresponds to the y coordinate of the center of the slit in Figure 2h. Note that the plots are marked with the y coordinate, not distance along the slit. Multiply the y coordinate by $\sqrt{2}$ for this roughly 45° slit to convert to distance.

The horizontal black lines in each panel mark the extent of the umbra. The ALMA data for $t1$-$t5$ are in Figure 2a, with gaps indicating times of no data due to calibrations. GST Hα center-line and blue-wing data are shown on the right (Figs 2b,d,f). IRIS 2796 Å slit-jaw data are shown in Figure 2c. AIA 304 Å and 171 Å data are shown in Figs 2e,f. Non-uniform chevron-shaped features (Kobanov et al. 2006) that tilt in the same direction can be seen in Figs 2b–g, suggesting an outward propagation towards the penumbra. The 3-minute oscillatory motion in these wavelengths also extends somehow into the penumbra (above or below the solid black lines in Figure 2a–g), but with some merging and increased separation to match the penumbral 5-minute oscillation period. This signature of propagation seems to be far less apparent in the ALMA data, and the oscillatory signature is only prominent in the umbra.

Our discovery of umbral oscillation in ALMA band 3 is groundbreaking in many respects. ALMA data provide a unique probe of temperature changes in the solar atmosphere in a relatively thin layer where the opacity is near unity (Loukitcheva et al. 2015). It is of interest to compare these oscillations in temperature with intensity oscillations provided by other instruments that probe different layers of solar atmosphere. Figure 3 compares the light curves obtained from a cut at $x = -251.0''$, $y = 222.5''$ in the time-distance plot (Figure 2) for multiple instruments. The location of the cut was chosen based on the wave patterns in all wavelengths shown in Figure 2 so that it covers the region of strongest oscillations. The data have been arbitrarily scaled and offset for better comparison. Though separated by gaps, we can still see some correspondence between light curves of different wavelengths, which enable the calculation of phase relations that will be discussed later.

In order to study the oscillation power, we applied the Fourier power spectrum for each pixel in both the ALMA map and GST image time series. Although the temporal resolution of ALMA (2 s) and GST (∼40 s) data are quite different, they both contain sufficient samples to resolve 3-minute oscillations and therefore can be used to measure the 3-minute oscillation power. The power spectrum was calculated as follows. For each ALMA (10-minute) solar scan, a map cube structure was made according to the method described above so the time series of each pixel can be easily obtained. The GST data were selected based on start and end time of each ALMA solar scan and made into map cube as well. Inspired by the method used in Ireland et al. (2015), the time series of each pixel in the ALMA and GST data cubes were obtained and normalized by $(I(t)) - \langle I(t)\rangle)/\langle I(t)\rangle$, where $I(t)$ is the varying brightness temperature for ALMA or vary-

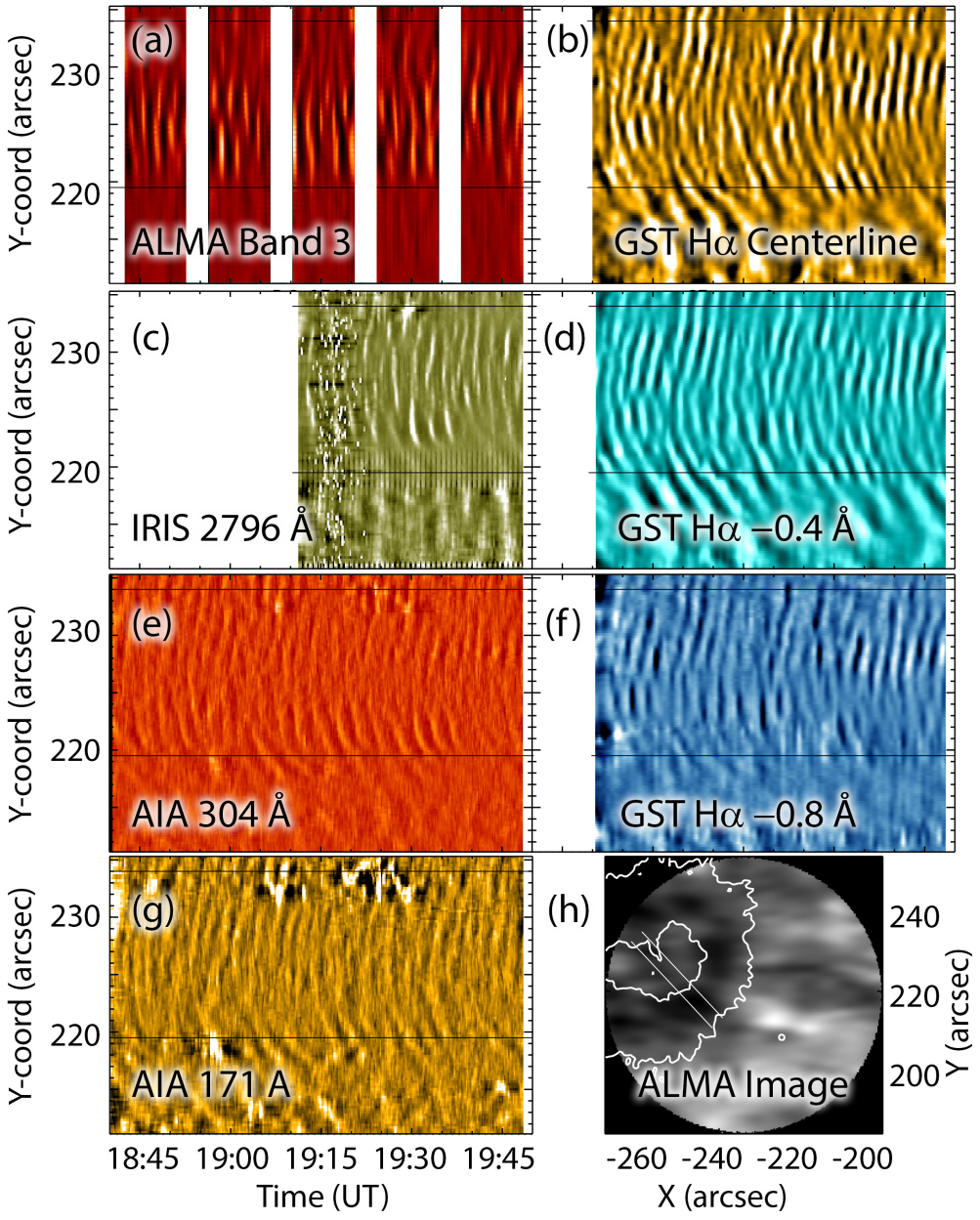

Figure 2. Time-distance plots based on the full duration of ALMA band 3 observation, 18:42:33-19:48:31 UT. An average of pixels between the two diagonal lines marked in panel (h) is used to constructed each time-distance plot. From (a) to (g): ALMA Band 3; BBSO GST Hα center line; IRIS 2796Å; BBSO GST Hα near blue wing (-0.4 Å); AIA 304Å; BBSO GST Hα far blue wing (-0.8 Å); AIA 171Å. The horizontal solid lines at y-offsets 219″ and 234″ mark the umbral boundaries, and the gaps between each ALMA band 3 time block are represented with white gaps. (h): ALMA image of sunspot NOAA 12470 with the boundaries of the slit and the contours from HMI image overlaid to show the umbral boundary.

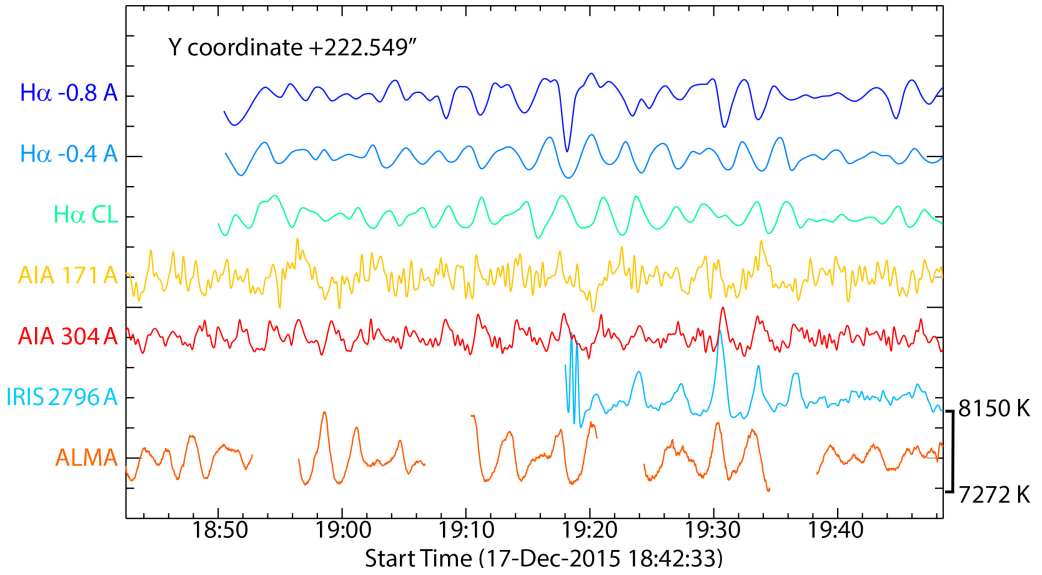

Figure 3. Light curves from an average over pixels between the two slit in Figure 2h at $x = -251.0''$, $y = 222.5''$. The point along the slit was chosen due to its good representation of the wave pattern. The name of instruments and observation band are on the left hand label, and the ALMA temperature range is shown with the scale on the right.

ing intensity for GST, and $\langle I(t) \rangle$ is the mean over each 10-minute ALMA scan.

A Hanning window was applied to the normalized time series to minimize edge effects. The full spatial resolution was retained during the process in order to reach the finest possible detail on the distribution of frequency-related physical contents as a function of location. We then applied the Fourier transform to the processed time series to form the power spectrum from each pixel. Figure 4 shows examples from three pixels in both the ALMA and GST Hα near blue wing (-0.4 Å) data cubes for time $t2$, one in the region of umbral oscillations, one in the penumbra, and one in the surrounding quiet Sun. No GST power spectrum could be obtained for the quiet Sun due to limited spatial coverage (see Figure 1b).

The differences in shape among these power spectra are consistent with what was seen in the ALMA time-distance plot in Figure 2a. The 3-minute band of the power spectra, which is the two closest bins to 0.0056 Hz marked with red dot-dashed lines, is especially strong for the umbral power spectrum. From Figure 4, we see that the peak of the umbral power spectrum is one to two magnitudes larger than the others in both data sets. The umbral spectrum of ALMA data also shows some evidence for harmonics near 0.015 Hz, which strongly suggests that the oscillation deviates from a sinusoid, as we demonstrate later. The frequency distribution of power is similar for the penumbra and quiet Sun.

To characterize the power spectrum spatial distribution, for each pixel we calculated the integrated power in the 3-minute band marked with the red dash-dot lines in Figure 4. This procedure was carried out for each 10-minute ALMA scan $t2$ to $t5$. The result for $t2$ is shown in Figure 5, where the 3-minute oscillation power is shown with red contours. Blue contours outline the umbral and penumbral boundary as seen in the HMI continuum image in panel (a).

We find that the strong 3-minute oscillation power falls solely inside the umbral boundary. The oscillations seem to be strongest in the western part of the umbra, while in the eastern region separated by a small light bridge structure, the 3-minute oscillations are present but weaker. This conclusion may be affected by the declining ALMA sensitivity at the edge of the primary beam, however.

To further compare the power spectra in different regions, we calculated the mean power for each frequency bin using all the pixels in the umbra, penumbra and quiet Sun to create the averaged power spectrum of ALMA t2 data for each region. A combination of two power-law functions, $af^b + cf^d$, was used in fitting the power-law tail starting from the frequency

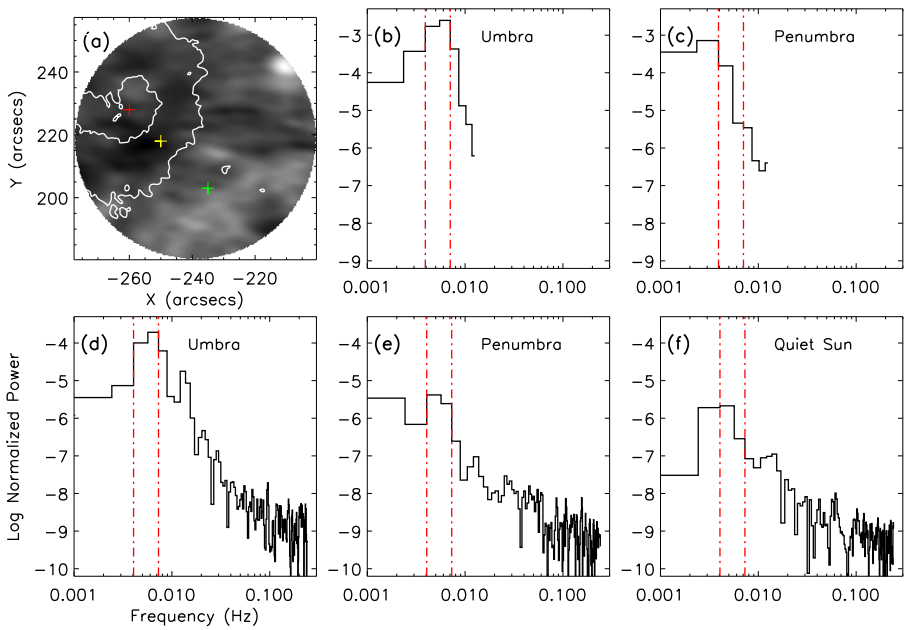

Figure 4. Three examples showing the power spectrum in the sunspot umbra, penumbra and quiet Sun regions. (a) ALMA image for locating the sample points, marked with plus signs. The inner white contour is the boundary of the sunspot umbra while the outer contour is the boundary for the sunspot penumbra. (b) Power spectrum of GST Hα near blue wing (-0.4 Å) data from red point in the sunspot umbra showing a strong peak in the 3-minute oscillation band marked with dot-dashed line. (c) The same as (b) for yellow point in the sunspot penumbra. (d) Power spectrum of ALMA data from the red point in the sunspot umbra. (e) (f) the same as (d) for sunspot penumbra and quiet Sun region.

bin immediately after the 3-minute range. The power-law index of the lower frequency term is shown in Figure 5 panel (b) - (d). The averaged penumbral power spectrum was overplotted using red lines on the umbral and quiet spectra for inter-comparison. The steeper slope shown in panel (b) by the blue dashed line reveals the influence of the high 3-minute power in umbral region, while the power-law indexes from the penumbra and quiet Sun are less steep. It is interesting that the umbral and penumbral high-frequency tail are essentially the same above 0.03 Hz (panel b), while the quiet Sun spectrum in panel (d) shows a notable excess near 0.03 Hz that contributes to a shallower and extended low-frequency slope. A red-noise spectrum above about 0.07 Hz is the same for all three regions, and may reflect residual fluctuations due to the Earth's atmosphere that have not been removed by the self-calibration procedure. Note that although the 5-minute oscillations cannot be well-resolved in the frequency domain, there is no sign of a peak near 0.0033 Hz in the penumbral spectrum of Figure 5c, which further confirms what we learned from the time-distance plots—that the penumbral 5-minute oscillations seen in Hα (Figure 2b,d) are not apparent in the ALMA band 3 data (Figure 2a).

Figure 6 shows the distribution of 3-min oscillation power in the $t2$ to $t5$ time ranges (columns) and all bands from ALMA and GST (rows). The rows represent the spatial evolution of the 3-min power for the wavelength band marked in the first column. The sunspot umbra is outlined in blue (see Figure 5) while the black contours with gray shading show the 3-min power maps of each data set. For a given band, the contour levels were set to be the same for $t2$ to $t5$, which are 10, 30, 50, 70 and 90 percent of the maximum value of oscillation power over the four power maps.

From Figure 6 we see that the shape of GST Hα far red wing (+0.8Å) 3-min power map contours is less organized and weaker than the others. While the other contours are generally constrained to lie well within the umbra, the power in the Hα far-red wing mainly lies along the umbral boundary. The relative amplitude of the +0.8Å power is also 5-50 times lower than in other bands, and hence we do not include it in our subsequent analysis.

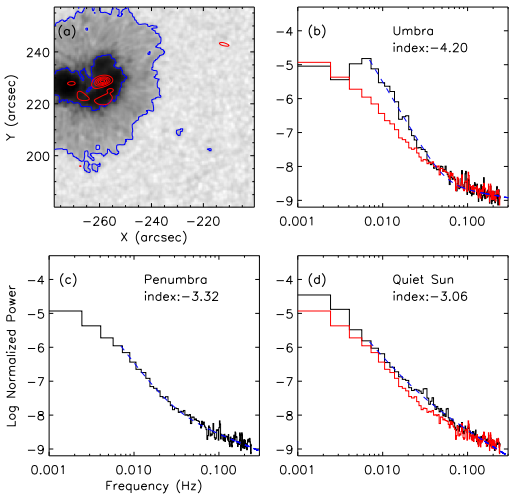

Figure 5. Comparison of ALMA power spectra averaged over umbral, penumbral, and quiet Sun regions. (a) HMI continuum image at 19:02 UT, overlaid with red contours showing the 3-min oscillation power and blue contours outlining the umbra and penumbra from the HMI continuum image. (b) Averaged umbral power spectrum with blue dashed line showing a region well fit by a power-law. (c) Same as (b) for the penumbral region. (d) the same as (b) for quiet Sun. The averaged penumbra power spectrum in panel (c) is over-plotted in red in both (b) and (d).

For the remaining bands, the 3-min power was in all cases strongest and most concentrated in $t2$ and reduced to 20-40% of that value in $t3$ to $t5$. Although it is difficult to tell from the shape and location of these contours, which suffer from the limited cadence of the Hα data, the overall pattern is consistent with the often seen appearance of new centers of oscillation power plus the lateral spreading of wave energy from previous centers (Yurchyshyn et al. 2020).

To determine the phase relationships among ALMA band 3 and GST Hα sub-bands, we plot in Figure 7 the light curves from these wavelengths taken in a region of high oscillation power (red plus symbol in Figure 6) and for comparison a neighboring region of low power (green plus symbol in Figure 6). The selected locations for the high power sample are different from $t2$ to $t5$, but within each given time block, the same position is used for every wavelength. The ALMA 2-s cadence data are plotted directly (black curve), while the lower-cadence Hα measurements are plotted in different symbols and colors, with the solid curves through the points showing the cubic spline interpolation to the ALMA cadence.

To better reveal the phase relationships among the different bands shown in Figure 7, we show five vertical dashed lines in the left column T3 panel that indicate the peak positions of the five light curves for one particular oscillation. The colors match the colors of light curves for the corresponding wavelengths. These dashed lines reveal a general sequence of the phase relationship, with Hα far blue wing (-0.8 Å or -0.08 nm) peaking first, then in order of peak time the Hα near blue wing (-0.4 Å), ALMA band 3 (100 GHz or 3.0 mm), Hα center line and Hα near red wing (+0.4 Å). We calculate the delay times based on these peak positions, relative to the Hα far blue wing to be 14 s, 32 s, 64 s and 82 s. This timing pattern is followed remarkably faithfully in the other individual oscillations in the left column, with similar time lags. Since the locations of the sample point in the umbra change in the different periods $t2$ to $t5$, the relatively stable phase shift between these bands suggests that it is a characteristic of the propagating waves that should be accounted for in any physical interpretation.

We also compared the light curves from the strong 3-min oscillation region in the left column with the ones from a nearby, relatively quiet umbral region (green plus symbols in each panel of Figure 6) in the right column for $t2$-$t5$. Unlike the case for the peak oscillation region, where the location is different for each time window, the quiet region selection is fixed for all of the time windows. For each time window, the amplitude range was scaled to match the left column to show the difference between these two regions. One can see that for $t2$, $t4$, and $t5$ ALMA temperature oscillations are not apparent when compared to the high-power region, although velocity fluctuations in the Hα bands still persist at a reduced level. In $t3$ the ALMA oscillations do appear in the quiet region, again at a reduced level. The significant differences in oscillatory power across the umbra, both in temperature and velocity diagnostics, indicate rapid spatial and temporal modification of the wave propagation characteristics.

In order to study the general phase relationships among all bands in the strong 3-min oscillation region, we performed an epoch analy-

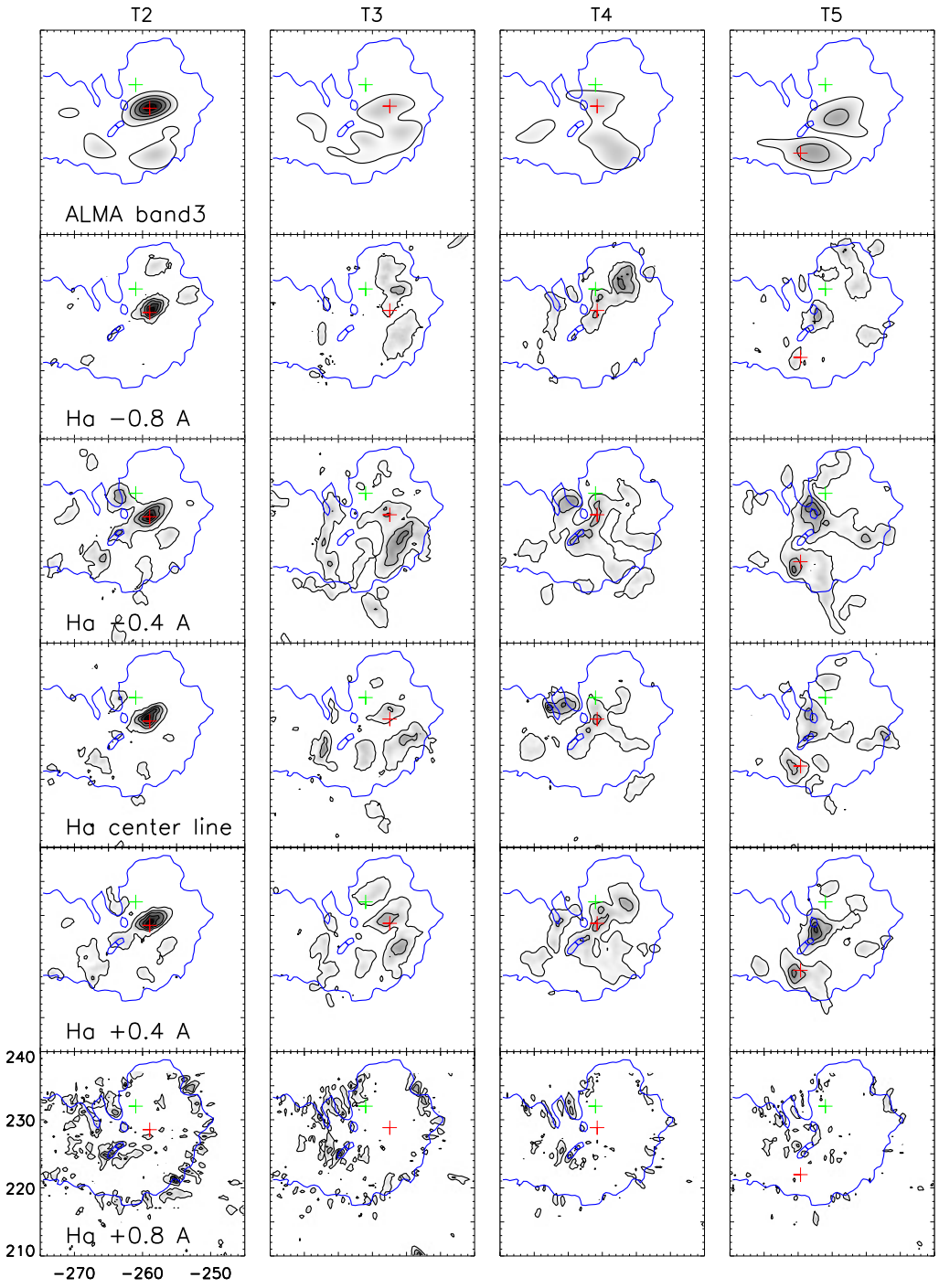

Figure 6. Spatial distribution and relative power level of 3-min oscillations in various bands. For this comparison the Hα data have been temporally interpolated and spatially smoothed to match the ALMA resolution. The contours in ALMA and the Hα sub-band images represent 10, 30, 50, 70 and 90 percent of the peak value of the 3-min oscillation power in each wavelength. Red and green plus symbols mark regions of high and low power, respectively, whose light curves are plotted in Figure 7.

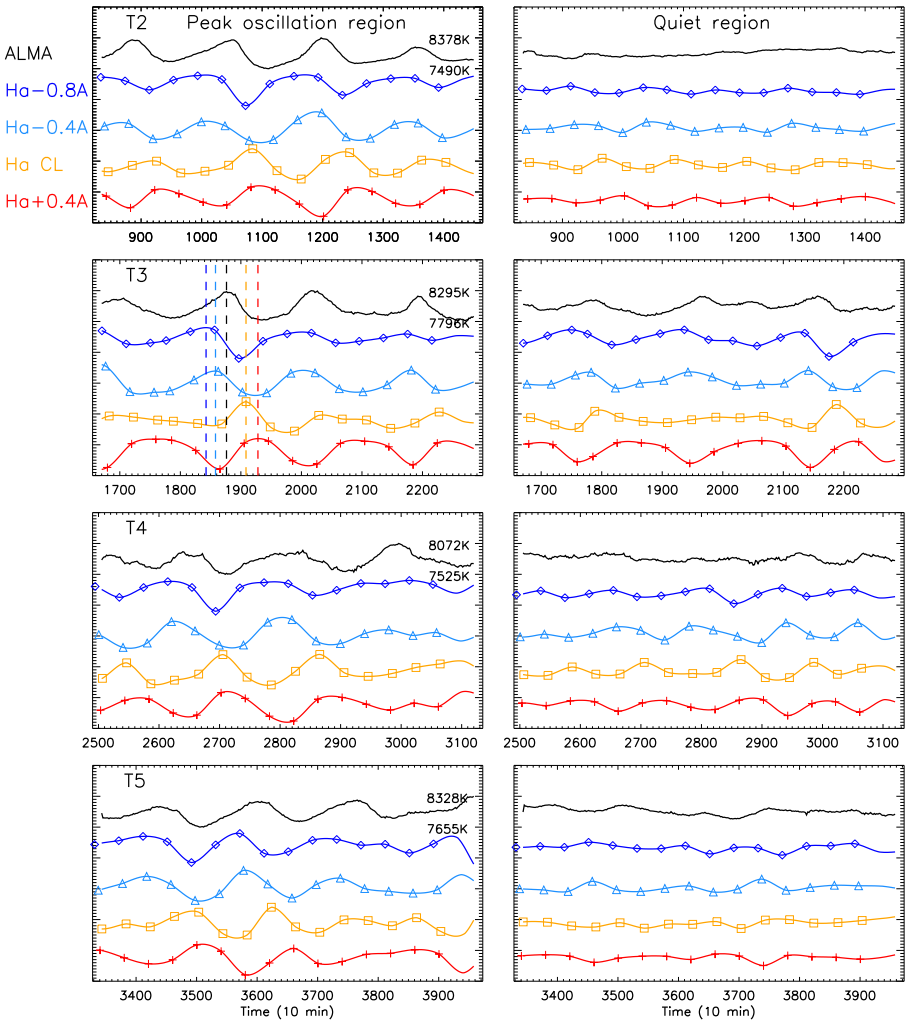

Figure 7. A comparison of light curves from pixels of strong oscillation (left column) and those from a relatively quiet region (right column) from locations marked with red and green plus sign in Figure 6. Different bands of ALMA and GST Hα data, which follow the same order top-to-bottom as in Figure 6, are plotted with different colors as shown by the labels adjacent to the upper-left panel. The time axis is marked in seconds, sequentially from the start time of the ALMA observations at 18:42:33UT. The dashed lines in $t3$ left column mark the peak times of these light curves for one particular oscillation, as discussed in the text. The ALMA maximum and minimum brightness temperatures are also shown in each left-hand panel, showing a fluctuation of ±250-500 K.

sis where individual oscillations are overlaid in terms of their phase relative to the peak of the Hα far blue wing (−0.8 Å). This was done for individual time windows $t2$ to $t5$ in the left column of Figure 8, with solid, dashed, and dotted lines for the first, second, and third oscillations in each time window, respectively, and for all time windows in the right column. The oscillations in different wavelengths were offset vertically for clarity, and the ALMA light curve was moved to the middle position to reflect its ordering of peak time midway between Hα near blue wing (−0.4 Å, cyan) and Hα center line (yellow).

The left column of Figure 8 shows that the oscillations in $t2$ are highly coherent for both the ALMA and GST data, reflecting the stronger oscillation power during that time window. The peak of the first wave (solid line) in each band in $t2$ is marked with a symbol to show the progression in phase of the peaks similar to the vertical dashed lines in Figure 7. The right panel of Figure 8, overlaying the curves from all the time blocks, shows that this general pattern persists for all of the oscillations although there is higher variability in some bands. The Hα near blue wing and ALMA oscillations are particularly coherent for most of the oscillations,

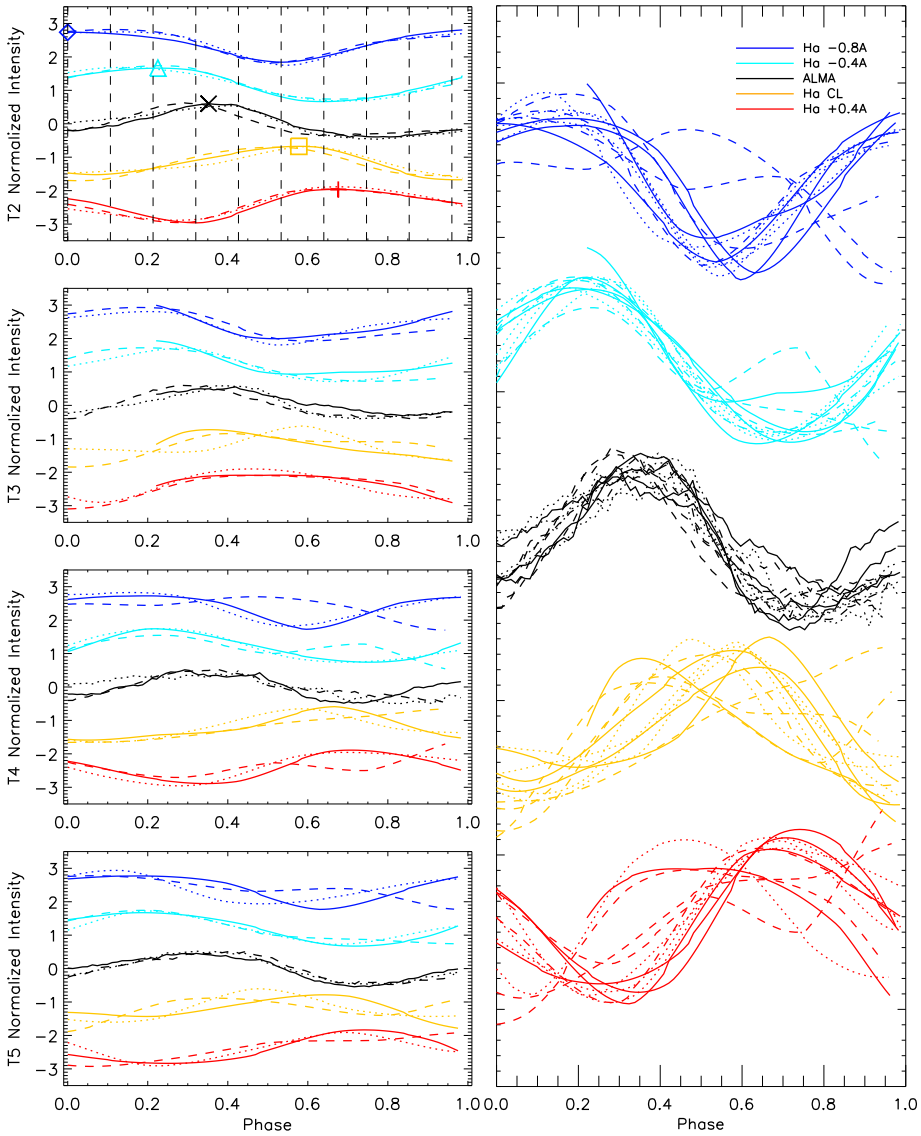

Figure 8. Epoch analysis of the relative phase of the oscillation pattern in different bands using the light curves from the strong oscillation region in the left column of Figure 7. Left panel: analysis for each ALMA time window separately. Each curve is offset vertically for clarity. The ALMA band 3 light curves (black) were moved to third place to best reflect the phase order. Each wave in the light curves is distinguished using different line styles (solid, dashed, and dotted line for the first, second, and third complete wave respectively). Right panel: an overlay of all waves from the left column.

and there is a marked tendency for the drop in ALMA brightness (corresponding to temperature) to be steeper than its rise.

4. DISCUSSION

In order to put the oscillations in temperature detected by ALMA into context with the wavelength-dependent brightness variations in the Hα line, and thus account for the phase shifts in Figures 7 and 8, a quantitative solar atmospheric model that exemplifies the sunspot structure is needed. Inspired by Molnar et al. (2019), we used the RH code (Rybicki & Hummer 1991, 1992; Uitenbroek 2000) to synthesize the chromospheric radiation in 1D, which uses the Solar Irradiance Physical Modeling (SRPM) as an input for the calculation (Fontenla et al. 2011). Due to the estimated formation height of ALMA band 3 (Loukitcheva et al. 2015), we used a sunspot umbral model (model S) that focuses on the photosphere and chromosphere (model index 1006). The RH code solves combined equations of statistical equilibrium and radiation

transfer for multi-level atoms and molecules under certain input parameters. The simulation was carried out with non-LTE setup for 6-levels of hydrogen atom (levels 0 to 5, plus the continuum), while other atomic species were treated with the LTE assumption. In addition to the default Hα output wavelength grid, we also used the RH code to produce the radiative emission in the wavelength range from 2.6 mm to 3.4 mm corresponding to the ALMA band 3 observations.

The results from the RH simulation of the umbra model are shown in Figure 9 for both wavelength ranges. The contribution functions are illustrated in the underlying gray scale map while the emergent intensities are plotted in violet lines. The Hα center line position was set to zero, and four dashed vertical lines indicate the sub-bands used in our study. From this result, we can see that the contribution function for Hα extends over a wide height range as seen on the left panel. The major part of the center line intensity comes from a narrow layer in the middle chromosphere ($\sim$ 1100 km) while the continuum is mainly formed in the photosphere. In the ALMA band 3 wavelength range, the formation height seen in the right panel is extended between 600 km and 1000 km in the chromosphere. Combined with the phase pattern indicated by the dashed vertical lines in Figure 7, we can conclude that the Hα line wing signatures are most likely dominated by the velocity of the waves, as observed by Phillis (1975).

To better understand the influence of the oscillation on the Hα line profile, we use the first complete oscillation in the $t2$ light curves to fit dynamic Hα line profiles. Because no photometric calibration is available for the GST data, we instead use the normalized values from each Hα sub-band light curve in the top-left panel of Figure 8 to calculate the relative variations at these four sub-bands at any given time. In this process, we assume that the line profile at Hα off-center bands can not exceed the continuum, so the light curves are obtained relative to the maximum values at these wavelengths. For the line center the relative variation is based on the mean value of its light curve. To anchor the continuum for the fits, two far off-center wavelengths (+/- 3 Å) were added to represent the continuum value, we then applied Gaussian fitting to these six points to form an interpolated line profile for a given time. To further stabilize the fits, only line width and line center position were allowed to change during the Gaussian fitting.

The result is shown in Figure 10. Each color in the color bar represents one of the vertical dashed lines in the top left panel of Figure 8, with numbers showing the order in time. The original simulation result from the RH code is also plotted with a dashed line in the figure, and is used to provide the intensity scale shown on the vertical axis. From the color-coded time bins in the figure we can form a schematic picture of how the Hα line profile changed with time/oscillation phase—it starts near the original dashed line profile, shifts to longer wavelengths (blue curves), then rapidly shifts to shorter wavelengths (green), and finally moves back to the center (red).

Although these fits are approximate, the behavior of the resulting line full-width half-maximum (FWHM) and line shift (Doppler velocity) shown in Figure 11 are suggestive. In the upper panel of Figure 11, we plot the temperature oscillation from ALMA alongside the line width information generated by the Gaussian fitting. Note that the line width varies in phase with the temperature variations measured by ALMA, with the greatest width corresponding to the highest temperature. This is consistent with the finding by Molnar et al. (2019) that ALMA temperature is correlated with Hα line width.

The lower panel of Figure 11 shows the Doppler velocity. The positive Doppler shift corresponds to the upward propagating waves. The maximum downward Doppler velocity amplitude is 3.4 km/s while the maximum upward velocity is 3.9 km/s. The asymmetric Doppler velocity profile reveals that the plasma moves downward slowly with a steady acceleration and then suddenly changes its direction and moves upward with a much larger acceleration, creating a steep rise in the velocity diagram.

The clear signature of a sawtooth pattern in the Doppler velocity for this particular oscillation, which is the largest amplitude one in our observations, has to be taken with some caution due to the relatively low cadence ($\sim$40 s) and small number of wavelengths (4) on which it is based. Even so, we find that both the Doppler velocity magnitude and trend in Figure 11 agree well with those reported by

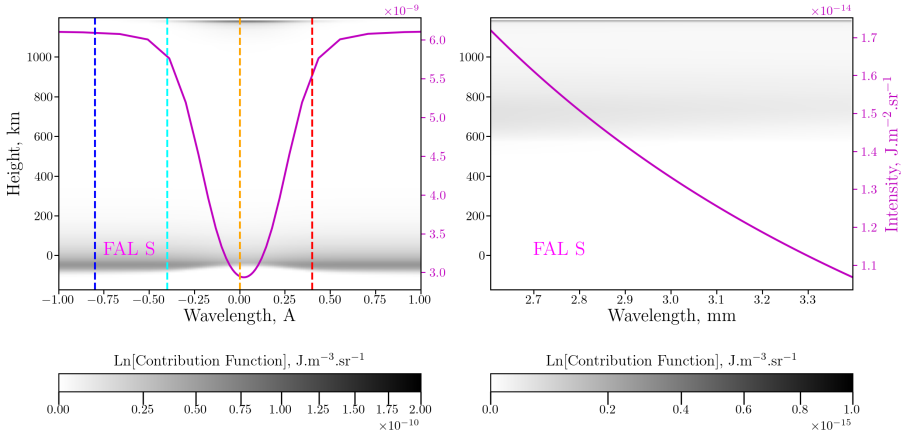

Figure 9. Spectral synthesis results obtained with the RH code. Left panel: Intensity contribution function (gray shade) vs. height for the Hα line from the FAL S model that simulates a sunspot umbra, overlaid with the emergent line profile (violet line, scale on the right axis). The wavelengths are shown relative to Hα line center, with four vertical dashed lines to indicate the Hα sub-bands used for the study. The line colors follow the same scheme as in Figures 7 and 8. Right panel: Contribution function for the emergent intensity for ALMA band 3 wavelength range from the same FAL S model, overlaid with the emergent intensity profile (violet line).

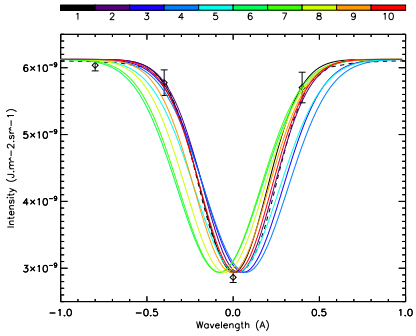

Figure 10. A series of interpolations of the Hα line profile in phase order based on the simulation result from RH code as well as the relative intensities of the four Hα sub-bands. The dashed line represents the original emergent line profile (violet line in Figure 9 left panel), while each colored line represents Gaussian fitting to the four Hα line intensities at 10 times (marked with 10 vertical dashed lines in Figure 8). The color bar indicates the time bin. For these fits we kept the continuum and line-core intensities fixed and fit only line shift and line width. The error bars plotted for the first Gaussian fit were calculated based on the standard deviation of the light curves in the nearby quiet region for each of the four Hα sub-bands.

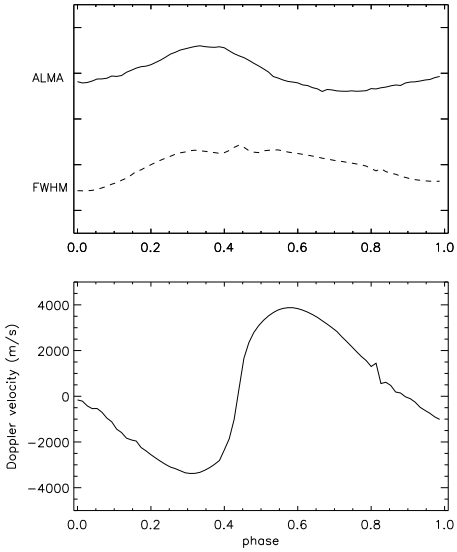

Figure 11. Top panel: A comparison between an ALMA light curve (first oscillation of $t2$) and full width at half maximum (FWHM) of the Gaussian fitting in Figure 10. Bottom panel: The Doppler velocity corresponding to the Hα center line shift in Figure 10. The upward Doppler velocity is treated as positive in the figure.

Tziotziou et al. (2006) and Chae & Litvinenko (2017). This asymmetrical Doppler velocity trend continues in observations of transition region lines (Tian et al. 2014), with a higher velocity of order 10 km s^{-1}. Such asymmetries are evidence of steepening or shock behavior in the atmosphere of sunspot umbrae, which was discovered in the Doppler shift of Ca II (Lites 1984) as well as He I (Lites 1986). In any case, the asymmetry in the ALMA temperature behavior (slow rise in temperature followed by a faster fall) is clearly established by our observations with 2-s cadence, as seen in each of the

individual oscillations in Figure 7 and in the right panel of Figure 8.

The ALMA temperature variation—its magnitude, phase relative to Hα Doppler velocity, and its asymmetric shape—all provide new information on the phenomenon of umbral 3-min oscillations. We have investigated whether these observations can be explained by current theories of acoustic wave propagation by performing a simulation from the model of Chae & Goode (2015). We compare the results of our simulations from their model with the observations, as shown in Figure 12. In brief outline, the steps we took to produce Figure 12b are (i) implementing their model in Python, (ii) using it to calculate the atmospheric parameter perturbations (velocity v, number density perturbation dn_e, and temperature perturbation dT) as a function of height and time, (iii) modifying the FAL umbral model by adding these perturbations as fractional changes at multiple time steps, and (iv) running the RH code at these multiple time steps to simulate the Hα line profile and ALMA brightness temperature. The good agreement of the phase differences between the observations (Figure 12a) and simulations (Figure 12b) suggest that the ALMA temperature variations are mainly a consequence of an upward propagating acoustic wave in the stratified medium of the sunspot umbra.

Similar to Figure 10, we plotted the temperature profile based on the simulated emergent intensity in band 3 wavelengths from the RH code at the 10 phases marked in Figure 12b. The colors from blue to red indicate increasing phase (or time), as shown in the color bar. The temperature profile starts at the lowest temperature, rises to the peak, and then falls back. The rapid line shift that happens between time bins 4 to 7 in Figure 10 corresponds to the temperature peak in Figure 13, but the earlier peak in the observations (Figure 12a) relative to the linear model (Figure 12b) suggests a tendency for the chromosphere to be heated more strongly at this time than described by the linear theory. The absolute temperature and temperature fluctuation predicted by the RH code, about 8700 K and ±1100 K, respectively at 3 mm, are both somewhat higher than the observations (Figure 7), which are around 8000 K and ±500 K. See Loukitcheva et al. (2017) for a detailed comparison of the brightness temperatures with various chromospheric models for this same sunspot observed one day earlier.

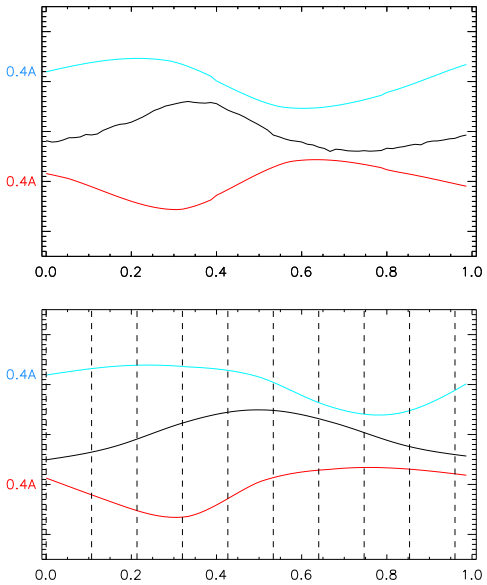

Figure 12. Comparison of (a) the observed H-alpha intensity in red and blue wing and ALMA temperature variation with (b) the same quantities from the hydrodynamic acoustic model of Chae & Goode (2015). Vertical dashed lines mark positions in phase similar to those in the top left panel of Figure 8

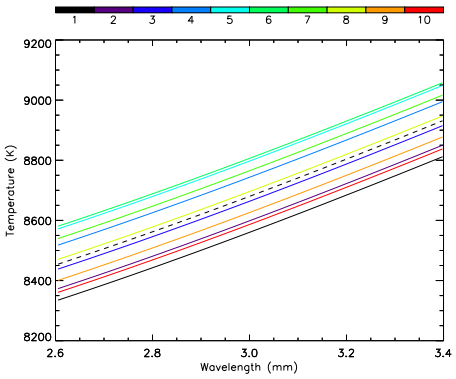

Figure 13. A series of ALMA temperature in phase order based on the simulation result from RH code. The dashed line represents the original temperature profile calculated based on the emergent line profile (purple line) in Figure 8 right panel. The color bar indicates the time bin. The temperature gradient reflects the fact that shorter wavelength of ALMA band3 sees deeper in the chromosphere.

5. CONCLUSIONS

Our study describes the first observations of sunspot oscillations detected by ALMA. The ALMA observations provide unique measurements of the chromospheric temperature variation tied to electron temperature via free-free emission, and so is relatively insensitive to atomic abundances and local non-equilibrium conditions.

We applied Fourier analysis to the ALMA band 3 data to create spatial maps of the 3-min power amplitude. The 3-min power maps correlate well to similar maps for all Hα sub-bands except the far red wing (+0.8 Å) where the 3-min oscillation signal is weak. From the light curves in Figures 7 and 8, we discovered a relatively constant phase relationship among Hα sub-band intensity and ALMA temperature as well as evidence for a sawtooth pattern in the ALMA temperature variation, albeit less abrupt than the velocity transition seen in Hα. The phase relationship among the different Hα bands sampling different parts of the line profile is consistent with a shift of the line center during the oscillation as well as a slight variation in line width. The ALMA temperature and the Hα line width peak at around the same time, but the ALMA temperature shows a more rapid fall after the peak time.

We used RH code to simulate the Hα line profile and the expected ALMA emission based on the FAL S sunspot atmosphere model. The results are generally in agreement with observations although the ALMA band 3 brightness temperature predicted by the FAL S model (8700 K) is some 9% greater than observed (8000 K). In order to understand the phase relationship of the observed ALMA temperature variation, we used the linear theory of Chae & Goode (2015) for the propagation of a hydrodynamic disturbance in a simplified solar atmosphere to obtain the velocity, density, and pressure perturbations as a function of height, then applied those perturbations to the FAL S model. Calculations of the Hα and ALMA emission using repeated runs of the RH code for different times during one oscillation of such a disturbance gave results that are in reasonable agreement with the model. In particular, the calculated relative phase relationships among the Hα near blue wing intensity, ALMA band 3 temperature, and Hα near red wing intensity are close to those observed, showing that the ALMA temperature variations are largely due to atmospheric heating expected for a propagating disturbance.

The symmetric temperature variation from the model is due to the linear theory used for wave propagation in Chae & Goode (2015) which cannot reproduce the slight sawtooth pattern observed in both the ALMA band 3 temperatures and Hα Doppler velocity, therefore a study of the non-linear solution for the wave function is much needed. Based on previous research (Litvinenko & Chae 2017; Chae & Litvinenko 2017), the non-linear effect can provide not only a physics scenario of the wavefront steepening and shock formation that is related with the sawtooth pattern, but also an explanation for the 2nd harmonic seen in the umbra power spectrum in Figure 4. We also note that the RH code gives an Hα line width for the FAL S model that is significantly narrower than commonly observed (Fricke & Elsässer 1965; Wallace et al. 2005). We have done a preliminary study of other models (e.g. the FAL penumbral model R and the Maltby model (Maltby et al. 1986), which can correct the Hα line-width discrepancy but results in estimated ALMA temperatures (and heights of formation) that are much too high. Here we simply note the discrepancy—a more thorough investigation will be addressed in a future paper now in preparation.

These new observations show the power of ALMA mm-wave observations for providing entirely new diagnostics of the solar atmosphere. Because of the low solar activity since these science-verification observations were made, no additional observations of sunspot umbrae have been possible to date. However, advances in ALMA capabilities for solar observations, such as higher spatial resolution, polarization, and additional frequency bands that provide diagnostics at both lower and higher heights, all offer great promise for investigations in the near future as solar activity returns. Such observations should motivate more sophisticated modeling that includes the effect of the hydrodynamic waves on ionization states as well as the effect of the strong sunspot magnetic fields.

This paper makes use of the following ALMA data: ADS/JAO.ALMA#2011.0.000020.SV. ALMA is a partnership of ESO (representing its member states), NSF (USA) and NINS

(Japan), together with NRC (Canada), MOST and ASIAA (Taiwan), and KASI (Republic of Korea), in cooperation with the Republic of Chile. The Joint ALMA Observatory is operated by ESO, AUI/NRAO and NAOJ.

BBSO operation is supported by NJIT and US NSF AGS-1821294 grant. GST operation is partly supported by the Korea Astronomy and Space Science Institute, the Seoul National University, and the Key Laboratory of Solar Activities of Chinese Academy of Sciences (CAS) and the Operation, Maintenance and Upgrading Fund of CAS for Astronomical Telescopes and Facility Instruments.

The National Radio Astronomy Observatory is a facility of the National Science Foundation operated under cooperative agreement by Associated Universities, Inc. YC gratefully acknowledges support from the NRAO Student Observing Support program.

The data used in this paper can be obtained from the following sources: The IRIS data can be obtained from https://iris.lmsal.com/data.html. GST data can be obtained from the BBSO data request form http://www.bbso.njit.edu/∼vayur/nst_requests2/. SDO data (AIA and HMI) can be obtained from http://jsoc.stanford.edu/.

REFERENCES

Anan, T., Schad, T. A., Jaeggli, S. A., et al. 2019, ApJ, 882, 161. doi:10.3847/1538-4357/ab357f

Bastian, T. S., Chintzoglou, G., De Pontieu, B., et al. 2017, ApJL, 845, L19. doi:10.3847/2041-8213/aa844c

Beckers, J. M. & Tallant, P. E. 1969, SoPh, 7, 351

Beckers, J. M. & Schultz, R. B. 1972, SoPh, 27, 61

Bogdan, T. J. & Judge, P. G. 2006, Philosophical Transactions of the Royal Society of London Series A, 364, 313. doi:10.1098/rsta.2005.1701

Cao, W., Gorceix, N., Coulter, R., et al. 2010, Astronomische Nachrichten, 331, 636. doi:10.1002/asna.201011390

Centeno, R., Collados, M., & Trujillo Bueno, J. 2006, Solar Polarization 4, 358, 465

Chae, J. & Goode, P. R. 2015, ApJ, 808, 118. doi:10.1088/0004-637X/808/2/118

Chae, J. & Litvinenko, Y. E. 2017, ApJ, 844, 129. doi:10.3847/1538-4357/aa7be9

Christopoulou, E. B., Georgakilas, A. A., & Koutchmy, S. 2000, A&A, 354, 305

Christopoulou, E. B., Georgakilas, A. A., & Koutchmy, S. 2001, A&A, 375, 617. doi:10.1051/0004-6361:20010887

De Pontieu, B., Title, A. M., Lemen, J. R., et al. 2014, SoPh, 289, 2733. doi:10.1007/s11207-014-0485-y

Felipe, T., Khomenko, E., & Collados, M. 2010, ApJ, 719, 357. doi:10.1088/0004-637X/719/1/357

Felipe, T., Kuckein, C., González Manrique, S. J., et al. 2020, ApJL, 900, L29. doi:10.3847/2041-8213/abb1a5

Fleck, B. & Deubner, F.-L. 1989, A&A, 224, 245

Fontenla, J. M., Harder, J., Livingston, W., et al. 2011, Journal of Geophysical Research (Atmospheres), 116, D20108. doi:10.1029/2011JD016032

Fricke, K. & Elsässer, H. 1965, Zeitschrift für Astrophysik, 63, 35

Giovanelli, R. G. 1972, SoPh, 27, 71

Ireland, J., McAteer, R. T. J., & Inglis, A. R. 2015, ApJ, 798, 1. doi:10.1088/0004-637X/798/1/1

Iwai, K., Loukitcheva, M., Shimojo, M., et al. 2017, ApJL, 841, L20. doi:10.3847/2041-8213/aa71b5

Khomenko, E. & Collados, M. 2015, Living Reviews in Solar Physics, 12, 6. doi:10.1007/lrsp-2015-6

Kobanov, N. I., Kolobov, D. Y., & Makarchik, D. V. 2006, SoPh, 238, 231. doi:10.1007/s11207-006-0160-z

Leibacher, J. W. & Stein, R. F. 1981, NASA Special Publication, 263

Lemen, J. R., Title, A. M., Akin, D. J., et al. 2012, SoPh, 275, 17. doi:10.1007/s11207-011-9776-8

Lites, B. W. 1984, ApJ, 277, 874. doi:10.1086/161758

Lites, B. W. 1986, ApJ, 301, 1005. doi:10.1086/163964

Litvinenko, Y. E. & Chae, J. 2017, A&A, 599, A15. doi:10.1051/0004-6361/201629568

Löhner-Böttcher, J., Bello González, N., & Schmidt, W. 2016, Astronomische Nachrichten, 337, 1040. doi:10.1002/asna.201612430

Loukitcheva, M., Solanki, S. K., Carlsson, M., et al. 2004, A&A, 419, 747. doi:10.1051/0004-6361:20034159

Loukitcheva, M., Solanki, S. K., Carlsson, M., et al. 2015, A&A, 575, A15

Loukitcheva, M. A., Iwai, K., Solanki, S. K., et al. 2017, ApJ, 850, 35. doi:10.3847/1538-4357/aa91cc

Maltby, P., Avrett, E. H., Carlsson, M., et al. 1986, ApJ, 306, 284. doi:10.1086/164342

Maurya, R. A., Chae, J., Park, H., et al. 2013, SoPh, 288, 73. doi:10.1007/s11207-013-0286-8

Mein, N. & Mein, P. 1976, SoPh, 49, 231. doi:10.1007/BF00162447

Molnar, M. E., Reardon, K. P., Chai, Y., et al. 2019, ApJ, 881, 99. doi:10.3847/1538-4357/ab2ba3

Nagashima, K., Sekii, T., Kosovichev, A. G., et al. 2007, PASJ, 59, S631. doi:10.1093/pasj/59.sp3.S631

Nindos, A., Alissandrakis, C. E., Gelfreikh, G. B., et al. 2002, A&A, 386, 658. doi:10.1051/0004-6361:20020252

Nindos, A., Alissandrakis, C. E., Bastian, T. S., et al. 2018, A&A, 619, L6. doi:10.1051/0004-6361/201834113

Nindos, A., Patsourakos, S., Alissandrakis, C. E., et al. 2021, A&A, 652, A92. doi:10.1051/0004-6361/202141241

Patsourakos, S., Alissandrakis, C. E., Nindos, A., et al. 2020, A&A, 634, A86. doi:10.1051/0004-6361/201936618

Petry, D. & CASA Development Team 2012, Astronomical Data Analysis Software and Systems XXI, 461, 849

Phillis, G. L. 1975, SoPh, 41, 71. doi:10.1007/BF00152957

Reardon, K. P., Lepreti, F., Carbone, V., et al. 2008, ApJL, 683, L207. doi:10.1086/591790

Reznikova, V. E., Shibasaki, K., Sych, R. A., et al. 2012, ApJ, 746, 119. doi:10.1088/0004-637X/746/2/119

Rybicki, G. B. & Hummer, D. G. 1991, A&A, 245, 171

Rybicki, G. B. & Hummer, D. G. 1992, A&A, 262, 209

Shibasaki, K. 2001, ApJ, 550, 1113. doi:10.1086/319820

Shimojo, M., Hudson, H. S., White, S. M., et al. 2017, ApJL, 841, L5. doi:10.3847/2041-8213/aa70e3

Skartlien, R., Carlsson, M., & Stein, R. F. 1994, Chromospheric Dynamics, 79

Su, J. T., Ji, K. F., Cao, W., et al. 2016, ApJ, 817, 117. doi:10.3847/0004-637X/817/2/117

Sych, R. & Nakariakov, V. M. 2014, A&A, 569, A72. doi:10.1051/0004-6361/201424049

Thomas, J. H. 1981, The Physics of Sunspots, 345

Tian, H., DeLuca, E., Reeves, K. K., et al. 2014, ApJ, 786, 137. doi:10.1088/0004-637X/786/2/137

Tziotziou, K., Tsiropoula, G., Mein, N., et al. 2006, A&A, 456, 689. doi:10.1051/0004-6361:20064997

Tziotziou, K., Tsiropoula, G., Mein, N., et al. 2007, A&A, 463, 1153. doi:10.1051/0004-6361:20066412

Uexkuell, M. V., Kneer, F., & Mattig, W. 1983, A&A, 123, 263

Uitenbroek, H. 2000, ApJ, 536, 481. doi:10.1086/308933

Wallace, L., Hinkle, K., & Livingston, W. C. 2005, An atlas of sunspot umbral spectra in the visible from 15,000 to 25,500 cm^{-1} (3920 to 6664 Å) , by Wallace, Lloyd.; Hinkle, Kenneth.; Livingston, W. C. [Tucson, AZ : National Solar Observatory, 2005]

Wedemeyer, S., Bastian, T., Brajša, R., et al. 2016, SSRv, 200, 1

White, S. M., Iwai, K., Phillips, N. M., et al. 2017, SoPh, 292, 88

Yurchyshyn, V., Abramenko, V., & Kilcik, A. 2015, ApJ, 798, 136. doi:10.1088/0004-637X/798/2/136

Yurchyshyn, V., Kilcik, A., Şahin, S., et al. 2020, ApJ, 896, 150. doi:10.3847/1538-4357/ab91b8

Zhugzhda, I. D. & Dzhalilov, N. S. 1982, A&A, 112, 16

Zhugzhda, I. D. 1984, MNRAS, 207, 731. doi:10.1093/mnras/207.4.731